

# A Statistical Assessment of Amortized Inference Under Signal-to-Noise Variation and Distribution Shift

Roy Shivam Ram Shreshth\*, Arnab Hazra\*, Gourab Mukherjee†

\*Department of Mathematics and Statistics,  
Indian Institute of Technology Kanpur, Kanpur, India 208016

† Marshall School of Business,  
University of Southern California, Los Angeles, United States 90089

January 14, 2026

## Abstract

Since the turn of the century, approximate Bayesian inference has steadily evolved as new computational techniques have been incorporated to handle increasingly complex and large-scale predictive problems. The recent success of deep neural networks and foundation models has now given rise to a new paradigm in statistical modeling, in which Bayesian inference can be amortized through large-scale learned predictors. In amortized inference, substantial computation is invested upfront to train a neural network that can subsequently produce approximate posterior or predictions at negligible marginal cost across a wide range of tasks. At deployment, amortized inference offers substantial computational savings compared with traditional Bayesian procedures, which generally require repeated likelihood evaluations or Monte Carlo simulations for predictions for each new dataset.

Despite the growing popularity of amortized inference, its statistical interpretation and its role within Bayesian inference remain poorly understood. This paper presents statistical perspectives on the working principles of several major neural architectures, including feedforward networks, Deep Sets, and Transformers, and examines how these architectures naturally support amortized Bayesian inference. We discuss how these models perform structured approximation and probabilistic reasoning in ways that yield controlled generalization error across a wide range of deployment scenarios, and how these properties can be harnessed for Bayesian computation. Through simulation studies, we evaluate the accuracy, robustness, and uncertainty quantification of amortized inference under varying signal-to-noise ratios and distributional shifts, highlighting both its strengths and its limitations.

**Keywords:** *Amortized Inference; Approximate Bayesian Computation; Distribution Shift; Generalization Error; Deep Learning;*

# 1 Introduction

Nearly twenty-five years ago, [Breiman \(2001\)](#) drew attention to a divide within statistical methodology between a data modeling culture, rooted in explicit probabilistic formulations, and an algorithmic modeling culture, which prioritizes predictive performance through flexible procedures that often lack a generative interpretation. While the former traditionally guided Bayesian analysis, the past two decades have seen a rapid expansion of high-dimensional and highly nonlinear models arising from machine learning, which increasingly influence Bayesian workflows and expand the set of problems for which fully probabilistic treatment is computationally feasible ([Shmueli, 2010](#)).

A major force behind this shift is the development of scalable Bayesian computation. Classical tools such as Markov chain Monte Carlo (MCMC) provide well-understood inferential guarantees ([Gelfand and Smith, 1990](#)). Still, they can become computationally prohibitive when applied repeatedly across large collections of related datasets or in models with expensive likelihoods. In many modern scientific pipelines, including climate modeling, astrophysics, genomics, and simulation-based inference, analysts must solve thousands or millions of Bayesian inverse problems within tight computational budgets. In such settings, the traditional per-instance paradigm of Bayesian computation becomes infeasible.

The concept of amortized Bayesian inference addresses this challenge by shifting the computational burden from inference at deployment time to a substantial, upfront training phase ([Gershman and Goodman, 2014](#)). Instead of running MCMC or optimizing a variational objective separately for each dataset, a flexible neural network is trained on a large collection of simulated or historical Bayesian inference tasks. Once trained, this network provides approximate posterior summaries, including point estimates, densities, or samples, for new datasets at negligible marginal cost. In effect, amortization constructs a global Bayesian surrogate, enabling rapid inference whenever new data arise from the same or a closely related generative mechanism. The benefits of amortization are well-illustrated by the training-deployment dynamics of modern large language models. For example, the BigScience Large Open-Science Open-access Multilingual Language Model (BLOOM) required more than a million GPU-hours on several hundred high-end processors during its four-month training phase, consuming an estimated 433.2 MWh of energy ([Luccioni et al., 2023](#)). As pointed out by [Zammit-Mangion et al. \(2025\)](#), this amount of energy is roughly equivalent to the annual usage of 70 Australian households. Once this substantial upfront cost is incurred, the trained model can generate high-quality text on a single GPU at a negligible computational and energy cost. This stark disparity between the cost of training and the efficiency of subsequent inference epitomizes the principle of amortization: a large, one-time computational investment yields an inference mechanism that can be applied repeatedly and efficiently across new inputs.

Amortized Bayesian inference has recently emerged as a powerful alternative to likelihood-based inference for complex data structures, including complex spatial and extreme-value models, where exact likelihoods are intractable or prohibitively expensive ([Sainsbury-Dale et al., 2024; Zammit-Mangion et al., 2025](#)). In spatial statistics, [Sainsbury-Dale et al. \(2025\)](#) have shown that neural Bayes estimators and graph neural-network-based amortized inferences can deliver fast, accurate inference for Gaussian and non-Gaussian spa-

tial fields, irregularly spaced data, and high-dimensional latent structures, dramatically reducing computation relative to classical Monte Carlo or Integrated Nested Laplace Approximation (Rue et al., 2009) approaches. In extreme-value analysis, where censored peaks-over-threshold models, heavy-tailed dependence, and spatiotemporal extremes yield challenging likelihood surfaces, amortized Bayesian inference has been employed to construct likelihood-free estimators, accelerate GEV-type Bayesian workflows, and facilitate inference under censoring and weak identifiability (Richards et al., 2024). Collectively, these developments demonstrate that amortized Bayesian inference provides a scalable and flexible framework for tackling the computational bottlenecks inherent in modern spatial and extreme-value modeling, offering near-instant, reusable inference once a simulator-trained network has been fit.

Neural amortization strategies can be broadly classified according to the type of Bayesian quantity they approximate. The first regime, direct neural point estimation, learns a deterministic mapping from data to parameter estimates. Although limited to first-order summaries, this approach is useful in likelihood-free or simulation-based settings where exact Bayesian computation is challenging. Architectures such as Deep Sets (Zaheer et al., 2017) and Set Transformers (Lee et al., 2019) provide principled methods for encoding symmetries inherent in the likelihood or prior structure. Neural posterior estimation (NPE) extends this idea by learning conditional density estimators for the posterior (Greenberg et al., 2019). The second regime, amortized variational inference (AVI), provides approximate posterior distributions rather than point estimates. These methods train neural networks to output parameters of an approximate posterior, effectively learning a variational family indexed by the data. Modern formulations often employ normalizing flows (Rezende and Mohamed, 2015; Papamakarios et al., 2021) to represent posteriors with complex curvature, skewness, and multimodality that cannot be captured by mean-field approximations (Radev et al., 2024). In Bayesian computation, AVI can be viewed as a simultaneous variational approximation over an entire distribution of tasks, rather than a single dataset. The third regime, neural samplers and transport methods, aims to accelerate Bayesian sampling by learning transformations that map complex posterior distributions to simpler latent distributions, where standard Monte Carlo procedures can mix rapidly. Neural transport maps (Hoffman et al., 2019) and flow-matching methods (Lipman et al., 2023) exemplify this approach. These techniques act as learned reparameterizations or preconditioners for MCMC, providing substantial computational savings in models with strongly correlated parameters or irregular posterior geometries.

The purpose of this paper is to assess these amortized approaches from a Bayesian perspective, with particular attention to their reliability, structural limitations, and empirical performance relative to classical computational methods. While amortization can offer significant gains in speed when the training distribution accurately represents the deployment environment, its accuracy and stability degrade once the generative mechanism deviates from the conditions encountered during training. To study this behavior systematically, we conduct extensive simulation experiments along three axes. First, we investigate training heterogeneity, examining how variations in task size and diversity influence posterior accuracy and calibration. Second, we study data-scarce deployment and quantify the dependence of amortized posteriors on effective sample size and signal-to-noise ratio. Third,

we evaluate robustness under distributional mismatch, characterizing how predictive and posterior accuracy deteriorate as covariates or structural aspects of the data-generating process drift from the training regime.

The paper proceeds as follows. Section 2 reviews the neural architectures employed: Feedforward Networks, Deep Sets, and Transformers, and clarifies their connection to Bayesian computation through kernel, variational, and transport-theoretic interpretations. Different aspects of amortized inference are summarized in Section 3. Section 4 presents simulation studies examining the three regimes described above under various signal-to-noise ratio and distributional mismatch setups. All code used to generate the results is provided at <https://github.com/Royshivam18/Neural-Amortized-Inference> to ensure full reproducibility. Section 5 summarizes the findings and highlights some future research directions.

## 2 Popular Neural Network Architectures

In this section, we discuss the modern neural network architectures typically employed within amortized inference pipelines. By establishing a clear analogy between these architectures and classical statistical methods, we aim to provide insight into why specific models are effective for particular inference tasks and how they can be interpreted beyond being merely black-box function approximators.

### 2.1 Feedforward Neural Networks

The Feedforward Neural Network (FNN), also known as a multilayer perceptron (MLP), serves as the foundational architecture for deep learning. It is a universal approximator capable of modeling complex nonlinear mappings between inputs and outputs.

The mathematical setup of FNN is as follows. Let  $L \in \mathbb{N}$  denote the network depth. We define the width of each layer as  $n_l$ , where  $l \in \{0, \dots, L\}$ . Consistent with our notation, the input dimension is  $n_0 = d_{\text{in}}$  and the output dimension is  $n_L = d_{\text{out}}$ . A (dense) feedforward neural network is a parametrized mapping  $f_\theta : \mathbb{R}^{d_{\text{in}}} \rightarrow \mathbb{R}^{d_{\text{out}}}$ , where  $\theta = \{(W^{[l]}, b^{[l]})\}_{l=1}^L$ , constructed on a strictly layered, acyclic computational graph with full connectivity between consecutive layers. Given an input vector  $x \in \mathbb{R}^{d_{\text{in}}}$ , the network computes its output through a sequence of recursive transformations. The computation begins by setting the initial activation equal to the input,  $a^{[0]} = x$ . For each hidden layer  $l = 1, \dots, L-1$ , the network forms an affine transformation of the previous layer's activations as

$$z^{[l]} = W^{[l]} a^{[l-1]} + b^{[l]}, \quad (1)$$

and then applies a nonlinear activation function  $\sigma^{[l]}$  component-wise to obtain

$$a^{[l]} = \sigma^{[l]}(z^{[l]}). \quad (2)$$

Here,  $W^{[l]} \in \mathbb{R}^{n_l \times n_{l-1}}$  and  $b^{[l]} \in \mathbb{R}^{n_l}$  in (1) denote the weight matrix and bias vector for layer  $l$ , respectively. An affine transformation of the last hidden-layer activation produces

the final output of the network:

$$f_\theta(x) = W^{[L]} a^{[L-1]} + b^{[L]}$$

typically without an additional nonlinearity.

The nonlinear activation functions  $\sigma^{[l]}$  in the hidden layers in (2) are critical to this formulation. For instance, the Rectified Linear Unit (ReLU), defined as  $\sigma(z) = \max(0, z)$ , restricts the network to piecewise linear functions. Without these nonlinearities, the entire network would collapse into a single linear transformation  $f_\theta(x) = W_{total}x + b_{total}$ , severely limiting its expressivity.

The complete parameter set  $\theta$  resides in the space  $\Theta = \prod_{l=1}^L (\mathbb{R}^{n_l \times n_{l-1}} \times \mathbb{R}^{n_l})$ , and the total number of scalar parameters is given by  $N_\theta = \sum_{l=1}^L n_l(n_{l-1} + 1)$ . This hierarchical composition of functions allows the FNN to construct highly complex decision boundaries from simple linear operations.

### 2.1.1 Universal Approximation and Adaptive Basis Functions

The utility of FNNs in statistical inference is rigorously grounded in the Universal Approximation Theorem. Seminal works by [Cybenko \(1989\)](#) and [Hornik \(1991\)](#) established that standard multilayer feedforward networks are universal approximators. Formally, let  $C(K)$  denote the space of continuous functions on a compact set  $K \subset \mathbb{R}^{d_{in}}$ . The theorem states that the set of functions representable by a neural network with at least one hidden layer and a non-polynomial activation function  $\sigma$  is dense in  $C(K)$  with respect to the supremum norm. That is, for any target function  $g \in C(K)$  and error tolerance  $\epsilon > 0$ , there exists a parameter configuration  $\theta$  such that

$$\sup_{x \in K} |g(x) - f_\theta(x)| < \epsilon.$$

While the theorem guarantees the existence of an approximating network, the geometric nature of this approximation is dictated by the specific choice of activation function.

Modern architectures predominantly utilize the ReLU activation function. The geometric intuition for ReLU networks is that of polygonal estimation. As shown by [Montufar et al. \(2014\)](#) and [Arora et al. \(2018\)](#), a ReLU network functions as a piecewise linear estimator. It implicitly partitions the input domain into a finite union of convex polytopes (linear regions). Within each polytope, the network is strictly affine. Consequently, a ReLU network approximates complex nonlinear manifolds by tiling them with flat polygonal facets, similar to how a three-dimensional mesh approximates a curved surface.

In contrast, classical activation functions like the logistic sigmoid,  $\sigma(z) = (1 + e^{-z})^{-1}$ , or the hyperbolic tangent,  $\sigma(z) = \tanh(z)$ , operate via smooth superposition. As established in the convergence rates derived by [Barron \(1993\)](#), networks using these smooth, bounded, sigmoidal functions approximate the target function by superimposing smooth ‘steps’ or ‘ridges’. Unlike the sharp boundaries of ReLU polytopes, these activations provide a differentiable approximation where nonlinearity arises from the smooth saturation of neurons ([Cybenko, 1989](#)).

We can regard the first hidden layer as learning a dictionary of feature maps denoted by  $\Phi(x) = (\phi_1(x), \dots, \phi_{n_1}(x))^\top$ , where each  $\phi_i(x) := \sigma(v_i^\top x + b_i^{[1]})$  is a nonlinear basis

function. The second hidden layer then computes weighted affine combinations of these features. Analytically, the network output can be written as a basis expansion given by

$$f_\theta(x) = c + \sum_{j=1}^{n_2} \beta_j \sigma((W_j^{[2]})^\top \Phi(x) + b_j^{[2]}),$$

where  $W_j^{[2]}$  denotes the  $j$ -th row of the weight matrix  $W^{[2]}$ . This expression clarifies that the network is learning a new family of basis functions  $\{\sigma((W_j^{[2]})^\top \Phi(x) + b_j^{[2]})\}_{j=1}^{n_2}$  built upon the first-layer dictionary, rather than using a fixed basis. Unlike classical nonparametric regression, where the basis (e.g., Fourier or spline) is fixed *a priori*, the FNN adaptively learns the basis parameters to represent the data structure best. This adaptive capability allows the FNN to emulate classical bases. Let  $\mathcal{G} = \{g_1, \dots, g_p\} \subset C(K)$  be any finite collection of continuous functions (a prescribed basis). By the universal approximation theorem, for any  $\epsilon > 0$ , there exist parameters such that

$$\sup_{x \in K} \left| f_\theta(x) - \sum_{j=1}^p \beta_j g_j(x) \right| < \epsilon.$$

Equivalently, there exists a partition of the hidden units into blocks  $\{\mathcal{I}_j\}_{j=1}^p$  such that each block realizes an approximation:

$$\tilde{g}_j(x) = \sum_{i \in \mathcal{I}_j} \alpha_i^{(j)} \sigma(v_i^\top x + b_i^{[1]}), \quad \sup_{x \in K} |g_j(x) - \tilde{g}_j(x)| < \epsilon/p.$$

The second layer learns coefficients to form  $\sum_j \beta_j \tilde{g}_j(x)$ . Hence, even if the first layer (dictionary) is fixed, a two-hidden-layer network can approximate any finite linear combination of target basis functions on  $K$ .

This perspective allows us to map FNNs directly to classical kernel methods. Suppose the first-layer parameters are randomized:

$$v_i \sim P_v, \quad b_i^{[1]} \sim P_b,$$

and only higher-layer weights are trained. Then, each feature  $\phi_i(x) = \sigma(v_i^\top x + b_i^{[1]})$  acts as a random feature (Rahimi and Recht, 2007). The induced kernel

$$k(x, x') := \mathbb{E}_{v,b}[\phi(x)\phi(x')]$$

is well-defined under  $P_v$  and  $P_b$ . Training the second-layer coefficients  $\{\beta_j\}_{j=1}^{n_2}$  with squared loss and  $\ell_2$ -penalty is equivalent to kernel ridge regression with kernel  $k$ . Moreover, Neal (1996) showed that if we place Gaussian priors  $\beta_j \sim \mathcal{N}(0, \tau^2)$  and let  $n_2 \uparrow \infty$  with appropriate scaling, the induced prior over functions converges to a Gaussian Process (GP) with covariance  $k$ . In this regime, the posterior mean predictor coincides with the GP regression estimator in kernel  $k$ .

The claim that neural networks learn useful basis functions is not merely theoretical; it is observable in practice. A striking example is the phenomenon of ‘Grokking’ (Power

et al., 2022), observed when training networks on algorithmic tasks like modular addition ( $a+b \bmod P$ ). Initially, the network memorizes the training data. However, after extended training, it generalizes perfectly. Mechanistic interpretability studies (Nanda et al., 2023) have revealed that in this generalized phase, the embedding layers explicitly converge to represent Fourier bases (sines and cosines). The network ‘discovers’ that the optimal basis for cyclic group operations is trigonometric, and it builds these bases from scratch using its weights to perform spectral analysis on the inputs.

## 2.2 Deep Sets as the Summary Statistic Machine

Standard FNNs are inherently limited when applied to statistical inference tasks involving sets of independent and identically distributed (IID) observations. A standard MLP requires a fixed-size input vector, yet datasets in inference tasks naturally possess variable cardinality. Furthermore, the joint probability of an IID set,  $p(x_1, \dots, x_N)$ , is invariant to permutations of the indices. Consequently, any estimator  $\hat{\theta}(x_1, \dots, x_N)$  derived from such data must respect this exchangeability. Standard architectures, which process inputs as ordered sequences, fail to capture this symmetry efficiently. To address this, Zaheer et al. (2017) proposed the ‘Deep Sets’ architecture, which provides a theoretically grounded framework for learning permutation-invariant functions.

Consider a set of inputs  $\mathcal{X} = \{x_1, x_2, \dots, x_N\}$  where each element  $x_j \in \mathbb{R}^{d_{\text{in}}}$ . The Deep Sets architecture processes this set through a three-stage mechanism to ensure permutation invariance. First, an embedding function (encoder)  $\phi : \mathbb{R}^{d_{\text{in}}} \rightarrow \mathbb{R}^{d_{\text{latent}}}$ , typically parameterized as an MLP, maps each individual element to a latent representation:

$$h_j = \phi(x_j), \quad j = 1, \dots, N.$$

Crucially, this mapping is applied identically to every element in the set, ensuring that the feature extraction is independent of the element’s position.

Subsequently, a permutation-invariant aggregation operator is applied to the set of latent codes  $\{h_1, \dots, h_N\}$ . While operators such as the mean or maximum are permissible, sum-pooling is often preferred in theoretical contexts as it preserves information regarding the set size  $N$ , which is vital for Bayesian inference. The aggregated summary statistic  $Z$  is computed as

$$Z = \sum_{j=1}^N h_j = \sum_{j=1}^N \phi(x_j).$$

Finally, a second neural network  $\rho : \mathbb{R}^{d_{\text{latent}}} \rightarrow \mathbb{R}^{d_{\text{out}}}$ , referred to as the decoder or regressor, processes the aggregated summary statistic to produce the final estimator

$$\hat{y} = \rho(Z).$$

Combining these steps, the complete Deep Sets estimator can be expressed in the compact form

$$f(\mathcal{X}) = \rho \left( \sum_{x \in \mathcal{X}} \phi(x) \right). \quad (3)$$

From a statistical perspective, this architecture acts as a neural generalization of the Method of Moments (MoM). In classical estimation, parameters  $\theta$  are estimated by equating empirical moments to theoretical moments. This estimation involves computing a vector of sample moments,  $\hat{m}_k = \frac{1}{N} \sum x_i^k$ , and applying an inverse mapping  $g$  to solve for  $\theta$ . The Deep Sets formulation mirrors this structure exactly: the encoder  $\phi(x)$  learns to extract optimal ‘generalized moments’ (sufficient statistics) rather than relying on fixed polynomial powers; the summation  $\sum \phi(x_i)$  accumulates these statistics into a fixed-size summary; and the outer network  $\rho$  approximates the inverse mapping  $g$ .

This analogy extends to the Moment Generating Function (MGF). The Taylor expansion of the MGF,  $M_X(t) = \mathbb{E}[e^{t^\top X}]$ , encapsulates all moments of the distribution. If the encoder  $\phi(x)$  possesses sufficient capacity, the aggregated vector  $\sum \phi(x)$  effectively approximates the MGF of the underlying empirical distribution. Since the MGF uniquely characterizes the distribution under mild conditions, a Deep Set that learns a sufficient number of these moments captures a finite-dimensional representation of the entire probability measure (Wagstaff et al., 2019). Theoretically, this principle is grounded in the Fisher-Neyman Factorization Theorem, which states that for Exponential Families, the likelihood factorizes through a sufficient statistic  $T(x)$ . Deep Sets effectively learn this statistic via  $\phi$ , making them ‘Neural Sufficient Statistic Learners’.

### 2.3 The Transformer as a Statistical Operator

Let  $X \in \mathbb{R}^{N \times d_{\text{model}}}$  denote the input sequence of embeddings, where  $x_j \in \mathbb{R}^{d_{\text{model}}}$  is the row vector corresponding to the  $j$ -th token. Each Transformer layer operates by projecting the input into three distinct subspaces: Queries ( $Q$ ), Keys ( $K$ ), and Values ( $V$ ). These projections are computed via learnable transformation functions  $\phi_Q$ ,  $\phi_K$ , and  $\phi_V$ . For each token  $x_j$ , the projections are defined as

$$q_j = \phi_Q(x_j), \quad k_j = \phi_K(x_j), \quad v_j = \phi_V(x_j),$$

where  $q_j$ ,  $k_j$ , and  $v_j$  denote the  $j$ -th row of the matrices  $Q$ ,  $K$ , and  $V$ , respectively. The mechanism then computes a pairwise similarity matrix  $S \in \mathbb{R}^{N \times N}$ , where each entry  $S_{ij} = \phi_Q(x_i) \phi_K(x_j)^\top$  represents the non-normalized alignment between the  $i$ -th query and the  $j$ -th key. To obtain a valid probability distribution over the sequence, these scores are scaled by  $1/\sqrt{d_k}$  and passed through a row-wise softmax function, yielding the attention matrix  $A$  with its  $(i, j)$ -th element being denoted by

$$A_{ij} = \frac{\exp(S_{ij}/\sqrt{d_k})}{\sum_{\ell=1}^N \exp(S_{i\ell}/\sqrt{d_k})}.$$

The final layer output  $Y$  is constructed as a weighted sum of the value vectors,  $Y_i = \sum_{j=1}^N A_{ij} v_j$ , or in matrix notation,  $Y = AV$ . In standard implementations, multiple such ‘heads’ are computed in parallel and concatenated to capture diverse dependencies (Vaswani et al., 2017).

The operation performed by the attention matrix  $A$  can be rigorously interpreted as a Nadaraya-Watson kernel regression estimator. We define an implicit, data-dependent

kernel function  $\kappa_\theta$ , parametrized by the projection weights  $\theta = \{W_Q, W_K\}$  as

$$\kappa_\theta(x_i, x_j) = \exp\left(\frac{(W_Q x_i)^\top (W_K x_j)}{\sqrt{d_k}}\right).$$

Unlike standard stationary kernels used in nonparametric statistics (e.g., the Radial Basis Function), which depend solely on the Euclidean distance  $\|x_i - x_j\|$ , this kernel is non-stationary. It effectively learns a metric space where the alignment of the learned features in the query-key subspace determines the similarity between them.

Under this definition, the attention weight  $A_{ij}$  is exactly the normalized kernel weight. The output  $Y_i$  then corresponds to the Nadaraya-Watson estimator of the function values  $V$  at the query location  $x_i$ , conditioned on the context set  $\{x_j\}$ :

$$Y_i = \mathbb{E}_{\hat{P}}[V \mid x_i] = \sum_{j=1}^N \frac{\kappa_\theta(x_i, x_j)}{\sum_{\ell=1}^N \kappa_\theta(x_i, x_\ell)} v_j. \quad (4)$$

Thus, statistically, the Self-Attention layer performs in-context kernel smoothing. It denoises and integrates information from the set of value vectors  $V$ , with the smoothing bandwidth and shape dictated dynamically by the learned similarity structure  $\kappa_\theta$  (Nadaraya, 1964; Watson, 1964).

This kernel smoothing interpretation invites a comparison to Gaussian Process (GP) regression. For a GP with kernel  $k(\cdot, \cdot)$  and noise variance  $\sigma_n^2$ , the posterior mean prediction for a test point  $x_*$  given training data  $(X, \mathbf{y})$  is given by  $m(x_*) = k(x_*, X)(K(X, X) + \sigma_n^2 I)^{-1}\mathbf{y}$ . While both architectures involve a weighted sum of targets, the Transformer differs fundamentally in its mixing mechanism. The GP posterior requires the inversion of the kernel matrix, an operation scaling as  $\mathcal{O}(N^3)$ . In contrast, the attention mechanism replaces this inversion with row-wise normalization (softmax), which scales as  $\mathcal{O}(N^2)$ . While normalization is only an approximation of the true posterior inverse, it allows the Transformer to scale to significantly longer sequences while retaining the capacity to model complex dependencies (Rasmussen and Williams, 2006).

The projection weights  $W_Q$  and  $W_K$  also admit a spectral interpretation via Mercer's Theorem. A valid Mercer kernel  $\kappa(x, x')$  can be decomposed into an eigenfunction expansion  $\sum \lambda_r \psi_r(x) \psi_r(x')$ . The Transformer approximates this infinite expansion with a finite-rank inner product of feature maps. Specifically, if we define the feature map  $\Phi(x) = xW$ , the attention score approximates the kernel via  $\Phi_Q(x_i)^\top \Phi_K(x_j)$  by

$$(x_i W_Q)(x_j W_K)^\top = \Phi_Q(x_i) \cdot \Phi_K(x_j)^\top.$$

Crucially, the use of distinct matrices  $W_Q \neq W_K$  generalizes the standard Mercer kernel. Classical covariance functions are strictly symmetric, implying  $k(x_i, x_j) = k(x_j, x_i)$ . However, the decoupled query-key projections break this symmetry. This projection offers the statistical flexibility to capture asymmetric dependencies, such as causal influence or temporal order, where the relevance of token  $j$  to token  $i$  does not imply the reverse relevance of token  $i$  to token  $j$ .

### 3 Amortized Bayesian Inference

Amortized Bayesian inference refers to a computational strategy where a significant initial computational budget is allocated to training a global model, allowing subsequent inference for individual test cases to become computationally efficient. This approach is particularly potent when combined with deep learning, replacing complex, iterative computational steps (such as MCMC or numerical optimization) with efficient forward passes of a neural network.

In many high-dimensional settings, such as image analysis or large-scale regression, the raw data  $x$  often contains redundant information. Neural networks allow us to compress  $x$  into lower-dimensional summary statistics, which classical statistical techniques can then leverage. In this work, we specifically focus on two complementary regimes of amortized inference: point estimation and uncertainty quantification.

#### 3.1 Point Estimation

In the first regime, the neural network acts as a direct function approximator for a statistical estimator. The goal is to learn a mapping  $f_\phi : \mathcal{X} \rightarrow \Theta$ , parameterized by weights  $\phi$ , that outputs a point estimate  $\hat{\theta}$  given observed data  $x$ . This formulation effectively reduces statistical inference to a supervised regression or classification problem.

To ensure the network approximates a valid Bayesian estimator, we employ a decision-theoretic framework. We define a loss function  $L(\theta, \hat{\theta})$  that quantifies the cost of estimating the true parameter  $\theta$  as  $\hat{\theta}$ . The goal is to minimize the Bayes risk, which is the expected loss over the joint distribution of the parameters and the data. Mathematically, let  $\pi(\theta)$  denote the prior distribution over parameters and  $p(x|\theta)$  the likelihood of the data. The Bayes risk,  $\mathcal{R}(\pi, f_\phi)$ , is defined as

$$\mathcal{R}(\pi, f_\phi) = \mathbb{E}_{\theta \sim \pi(\theta)} [\mathbb{E}_{x \sim p(x|\theta)} [L(\theta, f_\phi(x))]] , \quad (5)$$

or equivalently in integral form

$$\mathcal{R}(\pi, f_\phi) = \int_{\Theta} \int_{\mathcal{X}} L(\theta, f_\phi(x)) p(x|\theta) \pi(\theta) dx d\theta.$$

By minimizing this risk with respect to  $\phi$ , the neural network targets the Bayes estimator corresponding to the chosen loss function  $L$ . For instance, choosing the squared error loss  $L(\theta, \hat{\theta}) = \|\theta - \hat{\theta}\|^2$  dictates that the optimal function  $f_\phi^*(x)$  approximates the posterior mean,  $\mathbb{E}[\theta|x]$ .

##### 3.1.1 Implicit Topology Learning as Meta-Learning

The capability of a neural network to perform statistical inference is not merely a curve-fitting exercise; it represents a form of meta-learning. In traditional machine learning, a model learns to map a specific input,  $x$ , to a corresponding label,  $y$ . In this amortized inference regime, the network learns a functional mapping from an entire dataset  $\mathcal{D}_n = \{x_1, \dots, x_n\}$  to a parameter space  $\Theta$ .

This learning mechanism requires the network to internalize the topology of the parameter manifold. Rather than memorizing the answer for specific datasets, the network must learn the inductive biases of the generative model itself—effectively ‘learning how to estimate’. For example, when estimating the variance of a distribution, the network must implicitly learn that this parameter is strictly positive and correlates with the dispersion of the inputs, regardless of the specific values of the inputs.

This phenomenon is evidenced by the network’s behavior in the latent space. Much like Variational Autoencoders (VAEs) organize MNIST digits into smooth, continuous manifolds based on style and shape, a neural Bayes estimator organizes input datasets based on their statistical properties. It projects high-dimensional observations onto a lower-dimensional manifold that aligns with the true parameter space  $\Theta$ . This geometric alignment allows the network to generalize to unseen datasets generated from the same prior, effectively replacing the manually derived formulas of classical estimation (such as the ordinary least squares formula) with a learned, nonlinear equivalent.

## 3.2 Uncertainty Quantification

While point estimation provides a single best guess for the parameters, reliable statistical inference requires quantifying the stability and uncertainty of that estimate. In this second regime, we extend our evaluation to capture the variability of the inference process. We address this through two complementary approaches: a simulation-based bootstrap analysis to measure estimator consistency, and a fully Bayesian flow-based sampler for recovering the complete posterior distribution.

### 3.2.1 Bootstrap Stability Analysis

To rigorously evaluate the consistency of our neural estimator, we employ a simulation-based bootstrap procedure. Unlike classical bootstrapping, which resamples a single observed dataset, we leverage the generative nature of our experimental framework to assess estimator variance across repeated realizations of the data generation process.

For a fixed ground-truth  $p$ -length parameter vector  $\beta_{\text{true}}$  and a specific sample size  $N$ , we generate  $B$  independent datasets  $\mathcal{D}_1, \dots, \mathcal{D}_B$ , where each  $\mathcal{D}_b = \{(X^{(b)}, y^{(b)})\}$  for  $b = 1, \dots, B$ . These datasets represent potential realizations of the world under identical underlying laws but different noise instances.

We pass each dataset through the trained Transformer model to obtain a set of parameter estimates  $\{\hat{\beta}^{(1)}, \dots, \hat{\beta}^{(B)}\}$ . It is essential to note that our model employs a hard-thresholding mechanism to enforce sparsity; the network produces both a magnitude vector and an inclusion probability. The final estimate is computed as the element-wise product of the magnitude and a binary mask derived from the probabilities (thresholded at 0.5).

We quantify uncertainty by computing the standard deviation of these estimates across the  $B$  bootstrap replications. The empirical stability metric is defined as the average

standard deviation across all  $p$  coefficients:

$$\sigma_{\text{boot}}(N) = \frac{1}{p} \sum_{j=1}^p \sqrt{\frac{1}{B-1} \sum_{b=1}^B \left( \hat{\beta}_j^{(b)} - \bar{\beta}_j \right)^2}. \quad (6)$$

By evaluating the metric in (6) across varying sample sizes (e.g.,  $N \in \{50, \dots, 1000\}$ ), we can empirically verify the statistical consistency of the Transformer. A monotonic decrease in  $\sigma_{\text{boot}}$  as  $N$  increases confirms that the model effectively aggregates information from larger samples to reduce predictive uncertainty.

### 3.2.2 Flow-Based Posterior Sampling

While the bootstrap analysis quantifies the stability of the point estimate, it does not capture the whole geometry of the posterior distribution, particularly in multimodal settings. To address this, we employ a Flow Matching framework to train a neural network as a generative model that draws samples directly from the posterior  $p(\theta | x)$ . Further, to overcome the computational bottlenecks of traditional sampling, we leverage Conditional Flow Matching (CFM, [Lipman et al., 2023](#)). In contrast to MCMC samplers, which rely on local iterative updates to explore the parameter space, our flow-based mechanism learns a deterministic transformation from a simple base distribution to the complex target distribution.

The core premise is to identify a transformation capable of mapping samples from a tractable initial distribution  $p_0$  (e.g., a standard Gaussian) to the intractable target posterior  $p_1$ . Flow matching models this transformation by identifying an ideal vector field that dictates the optimal movement of probability mass from the initial state to the final state over a time horizon  $t \in [0, 1]$ .

We define a time-dependent vector field  $v_t : \mathbb{R}^d \rightarrow \mathbb{R}^d$  parameterized by a neural network with parameters  $\phi$ . The evolution of a sample  $z_t$  is governed by the ordinary differential equation

$$\frac{dz_t}{dt} = v_t(z_t; \phi).$$

By integrating this derivative from  $t = 0$  to  $t = 1$ , the neural network effectively transports samples from the prior directly to the posterior.

During training, we regress the neural vector field  $v_t$  against a conditional target vector field  $u_t$ . We select the Optimal Transport path, which creates a straight-line trajectory between a noise sample  $z_0$  and a data sample  $z_1$ . The loss function minimizes the discrepancy between the learned field and this ideal trajectory

$$\mathcal{L}_{\text{CFM}}(\phi) = \mathbb{E}_{t, z_0, z_1} \left[ \|v_t(z_t) - (z_1 - z_0)\|^2 \right]. \quad (7)$$

This approach effectively amortizes the inference cost: once the ideal vector field is learned, sampling becomes a fast, non-iterative forward pass of the ODE solver, avoiding the slow mixing and mode-collapse issues often encountered with MCMC in complex topologies.

## 4 Experimental Evaluation

### 4.1 Experiment I: Latent Structure Recovery

We study task heterogeneity through a clustered task prior and evaluate whether permutation-invariant neural estimators can amortize inference by learning shared latent structure across tasks. Concretely, we construct a meta-learning environment where each task corresponds to a linear regression problem with a task-specific coefficient vector  $\beta_t \in \mathbb{R}^p$ , but the collection  $\{\beta_t\}$  is constrained to lie on a finite set of latent centroids. We compare two amortized estimators, Deep Sets and Set Transformer, against a classical per-task estimator.

**Generative process.** We fix the feature dimension  $p = 20$  and the number of latent clusters  $K$ . We first sample  $K$  latent centroids following  $\mu_k \sim \mathcal{N}(0, \tau^2 I_p)$ ,  $k = 1, \dots, K$  with  $\tau = 3.0$ . These centroids remain fixed for the entire experiment and define a latent task mixture. For each task  $t$ , we sample its regression coefficient vector by selecting one centroid uniformly at random, i.e.,  $\beta_t \sim \text{Uniform}(\{\mu_1, \dots, \mu_K\})$ . Conditioned on  $\beta_t$ , we generate a task support set  $\mathcal{D}_t = \{(x_{t,n}, y_{t,n})\}_{n=1}^{N_t}$  with random support size  $N_t \sim \text{Discrete - Uniform}\{10, 11, \dots, 30\}$ . We sample the inputs as  $x_{t,n} \stackrel{\text{IID}}{\sim} \mathcal{N}(0, I_p)$  and outputs follow the linear model

$$y_{t,n} = x_{t,n}^\top \beta_t + \varepsilon_{t,n}, \quad \varepsilon_{t,n} \stackrel{\text{IID}}{\sim} \mathcal{N}(0, \sigma^2), \quad \sigma = 1.$$

**Training and test meta-datasets.** For each choice of  $K \in \{5, 10, 50\}$ , we independently generate a training meta-dataset of  $T_{\text{train}}$  tasks and a test meta-dataset of  $T_{\text{test}} = 200$  held-out tasks using the same generative process (i.e., the same  $K$  and hyperparameters). The neural models are trained across tasks to learn an amortized mapping

$$f_\theta : \mathcal{D}_t \mapsto \widehat{\beta}_t \in \mathbb{R}^p,$$

where  $f_\theta$  is expressed as either a Deep Sets encoder or a Set Transformer encoder followed by a regression head. Both architectures operate on the set of paired observations  $\{(x_{t,n}, y_{t,n})\}_{n=1}^{N_t}$  and are therefore permutation-invariant in the ordering of samples within a task.

**Baselines and evaluation metric.** As a classical baseline, we compute a per-task Ordinary Least Squares (OLS) estimate  $\widehat{\beta}_t^{\text{OLS}}$  using only the support set  $\mathcal{D}_t$ . We evaluate all estimators on the test tasks using parameter estimation error

$$\text{MSE}_\beta = \frac{1}{T_{\text{test}}} \sum_{t=1}^{T_{\text{test}}} \left\| \widehat{\beta}_t - \beta_t \right\|_2^2, \quad (8)$$

and train neural models for 100 epochs by minimizing the same objective over training tasks.

**Parameter estimation error.** We present the results on parameter estimation error in the latent structure recovery experiment in Table 1, which indicate that the neural networks perform exceptionally well in uncovering the hidden latent structure. While the OLS baseline yields consistently high error due to its inability to leverage the shared geometry of the tasks, both standard neural architectures achieve substantially lower error rates. In low-complexity regimes ( $K = 5, 10$ ), the networks effectively approximate the Bayes-optimal estimator. Even as the complexity increases to  $K = 50$ , both architectures continue to demonstrate robust generalization, confirming their ability to exploit the finite cluster structure of the parameter space.

Table 1: Parameter estimation error ( $\text{MSE}_\beta$  in (8)) in the latent structure recovery experiment. Results are averaged over 200 held-out test tasks. For OLS, we consider a per-task ordinary least squares estimator trained independently on each task using only its support set. For Deep Sets and Set Transformer, we consider amortized estimators trained across tasks.

Latent complexity	OLS (per-task)	Deep Sets	Set Transformer
Clusters ( $K = 5$ )	$1.46 \times 10^5$	0.477	<b>0.351</b>
Clusters ( $K = 10$ )	$1.37 \times 10^5$	1.663	<b>0.987</b>
Clusters ( $K = 50$ )	$3.96 \times 10^3$	9.301	<b>7.112</b>

## 4.2 Experiment II: Distributional Robustness

We next study the behavior of amortized estimators for large epochs and their robustness to distributional mismatch. This experiment jointly evaluates (i) sample complexity at the data-scarce frontier and (ii) stability under increasingly non-Gaussian noise distributions. Unlike Experiment I, where task heterogeneity is induced through a clustered prior, here tasks are independently generated but exhibit substantial within-task uncertainty due to high-variance parameters and complex residual structure.

**Generative process.** We fix the feature dimension  $p = 20$ . For each task  $t$ , we draw regression coefficients independently from a high-variance prior  $\beta_t \stackrel{\text{IID}}{\sim} \mathcal{N}(0, 9^2 I_p)$ . Conditioned on  $\beta_t$ , we generate a support set  $\mathcal{D}_t = \{(x_{t,n}, y_{t,n})\}_{n=1}^{N_t}$  with inputs sampled as  $x_{t,n} \stackrel{\text{IID}}{\sim} \mathcal{N}(0, I_p)$ . We generate outputs according to the linear model

$$y_{t,n} = x_{t,n}^\top \beta_t + \varepsilon_{t,n},$$

where the noise distribution  $\varepsilon_{t,n}$  varies across regimes described below.

**Noise regimes.** To assess robustness to distributional mismatch, we consider four residual distributions:

- Gaussian (symmetric):  $\varepsilon_{t,n} \sim \mathcal{N}(0, 1)$ .

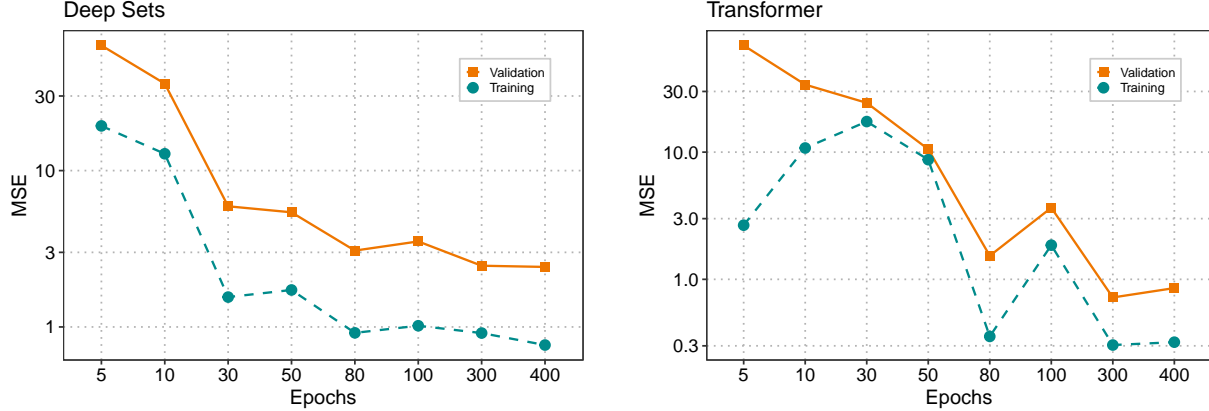


Figure 1: Comparative Learning Dynamics: The dashed lines represent model fit on training tasks, while solid lines indicate generalization error on unseen tasks. Deep Sets (Left) exhibits high efficiency for Epoch  $< 50$  but plateaus quickly. In contrast, the Transformer (Right) requires more epochs (Epoch  $> 80$ ) to stabilize but achieves significantly lower final error.

- Asymmetric:  $\varepsilon_{t,n} \stackrel{d}{=} E - 1$ , where  $E \sim \text{Exp}(1)$ .
- Bimodal:  $\varepsilon_{t,n}$  follows a two-component Gaussian mixture with weights  $\{0.8, 0.2\}$ .
- Trimodal:  $\varepsilon_{t,n}$  follows a three-component Gaussian mixture with weights  $\{0.8, 0.1, 0.1\}$ .

For the multimodal cases, component-specific means and variances are chosen to ensure well-separated modes, inducing heavy-tailed and non-convex error distributions.

**Training and evaluation protocol.** We first generate a fixed meta-dataset of  $T = 6000$  tasks using the generative process above. This meta-dataset is then split into  $T_{\text{train}} = 5400$  training tasks and  $T_{\text{test}} = 600$  held-out test tasks. We train the amortized estimators (Deep Sets and Set Transformer) on the training tasks for a fixed number of optimization epochs.

To study learning dynamics with increasing epochs, we evaluate the models at multiple training checkpoints (epochs)  $e \in \{5, 10, 30, 50, 80, 100, 300, 400\}$ , and report performance on the held-out test tasks. Robustness to distributional mismatch is assessed by evaluating the same trained model under each residual regime (Gaussian, Asymmetric, Bimodal, and Trimodal) while keeping the task prior and the task sample size distribution fixed.

**Objective and metrics.** As in Experiment I, Deep Sets and Set Transformer architectures learn an amortized mapping  $f_\theta : \mathcal{D}_t \mapsto \widehat{\beta}_t \in \mathbb{R}^p$ . We evaluate the performance using the parameter estimation error  $\text{MSE}_\beta = \mathbb{E} \left[ \|\widehat{\beta}_t - \beta_t\|_2^2 \right]$ , computed over held-out tasks and averaged across noise regimes and support sizes.

**Training Dynamics.** Figure 1 illustrates the training and validation performance of Deep Sets and the Set Transformer as a function of training epochs. Both panels report mean squared error evaluated on a fixed held-out validation set at selected checkpoints (epochs  $\{5, 10, 30, 50, 80, 100, 300, 400\}$ ). The horizontal axis, therefore, reflects the progress of optimization over training time, rather than the variation in the number of observations per task.

Deep Sets (left panel) exhibits rapid improvement during the early stages of training, with both training and validation error decreasing sharply within the first 30–50 epochs. Beyond this point, validation performance stabilizes and shows only marginal improvement with further training, indicating early convergence of the model under the chosen optimization settings.

In contrast, the Set Transformer (right panel) exhibits slower and less stable convergence in the initial epochs, characterized by higher validation error and greater variance during the early stages of training. However, continued optimization leads to sustained performance gains, and at later checkpoints (epochs 300–400), the Transformer achieves substantially lower validation error than Deep Sets. This behavior highlights differences in training dynamics: while Deep Sets converges quickly, the Set Transformer benefits more strongly from extended training and ultimately reaches a better-performing solution.

**Robustness to complex noise distributions.** We evaluate the robustness of the amortized estimators when the noise distribution at evaluation time deviates from the assumptions used during training. This analysis examines how robustness to distributional mismatch evolves as a function of training progress, while maintaining the data-generating process and evaluation protocol constant.

Neural models are trained under a Gaussian noise assumption and evaluated on held-out tasks generated under four distinct residual regimes: *Gaussian* (symmetric), *Asymmetric* (shifted exponential), *Bimodal*, and *Trimodal* (Gaussian mixtures). Model performance recorded at multiple training checkpoints  $e \in \{10, 50, 100, 500\}$  allow us to examine how robustness to increasingly complex noise structures improves with continued optimization.

Table 2 reports parameter estimation error, measured as mean squared error between the estimated coefficients  $\hat{\beta}_t$  and the ground truth  $\beta_t$ , averaged over held-out tasks. This metric directly reflects the sensitivity of the estimators to noise-induced perturbations under different residual distributions. Across all noise regimes, both architectures exhibit decreasing estimation error as training progresses, indicating improved robustness with continued optimization. Deep Sets achieves substantial gains early in training but shows slower improvement at later epochs. In contrast, the Set Transformer continues to benefit from extended training, consistently achieving lower errors at later checkpoints across all noise regimes. Notably, the relative ordering of performance across noise distributions remains stable throughout training, suggesting that the Set Transformer maintains robustness even under pronounced distributional mismatch.

As shown in Figure 2, we assess the stability of the amortized estimators by measuring bootstrap uncertainty as a function of the support set size  $N$ . Here,  $N$  denotes the number of observations provided to the model for a single task at inference time and should be clearly distinguished from the size of the training dataset or the number of training epochs.

Table 2: Parameter estimation error ( $MSE_{\beta}$ ) under distributional noise mismatch. Models are trained under Gaussian noise and evaluated on held-out tasks at different training epochs. Lower values indicate more accurate recovery of the true coefficient vector  $\beta_t$ .

Deep Sets ( $MSE_{\beta}$ )				
Noise Regime	Epoch 10	Epoch 50	Epoch 100	Epoch 500
Gaussian	39.7563	7.3948	4.6967	3.6488
Asymmetric	39.3615	8.4446	5.0542	3.6221
Multimodal	41.5351	7.6981	6.1458	4.3488
Set Transformer ( $MSE_{\beta}$ )				
Noise Regime	Epoch 10	Epoch 50	Epoch 100	Epoch 500
Gaussian	30.7624	14.5427	4.9565	0.8148
Asymmetric	34.0305	13.2421	4.8801	0.7987
Multimodal	32.1819	14.0616	4.6674	0.9633

For each task and noise regime, we perform bootstrap resampling over the support set and compute the standard deviation of the resulting parameter estimates. This quantity captures the sensitivity of the estimator to sampling variability and provides a direct measure of predictive stability. Both architectures exhibit a clear monotonic decrease in bootstrap standard deviation as  $N$  increases, indicating that parameter estimates become more stable as additional evidence is provided. This behavior is consistent with that of well-behaved statistical estimators, where the uncertainty decreases as the information content of the observed data increases. Notably, the Set Transformer demonstrates substantially lower uncertainty across all noise regimes and support sizes. In particular, its bootstrap deviation remains below 0.6 even in low-data settings, whereas Deep Sets exhibits considerably higher variability, with deviations exceeding 1.5 for small  $N$ . Moreover, the Transformer’s uncertainty curves for Gaussian, asymmetric, and multimodal noise remain closely aligned, suggesting that its stability is largely insensitive to the form of the noise distribution. This observation indicates that the attention-based architecture produces more reliable and consistent parameter estimates under both data scarcity and distributional mismatch.

### 4.3 Experiment III: Sparse Signal Recovery

To further probe Regime II (the data-scarce frontier), we study the recovery of sparse signals in high-dimensional linear regression. Each task corresponds to estimating a task-specific sparse coefficient vector from a small set of observations. Our goal is to learn an amortized, permutation-invariant estimator that identifies both the support and magnitudes of the sparse signal.

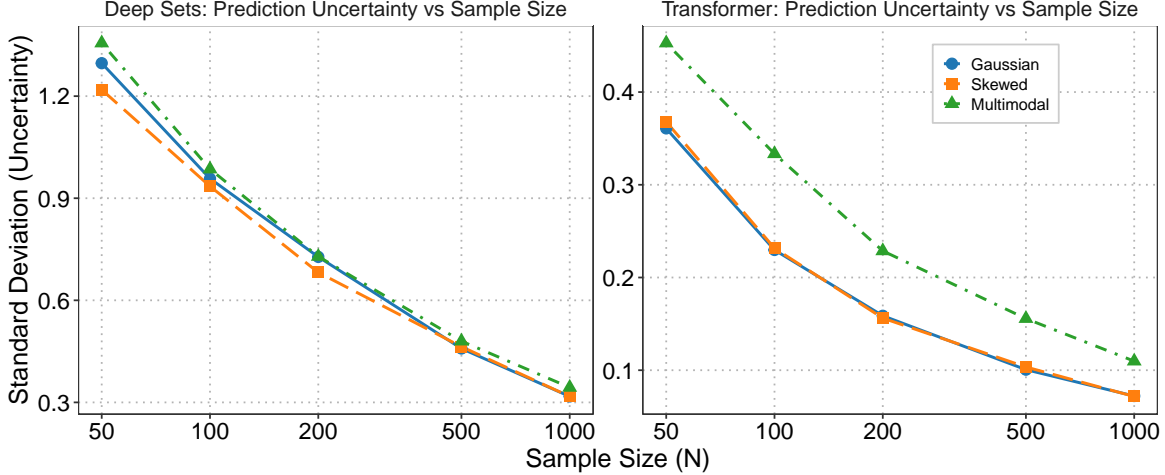


Figure 2: Bootstrap uncertainty convergence. Standard deviation of the estimated regression coefficients (computed via bootstrap resampling of the task support set) as a function of support set size  $N$ . Both architectures exhibit decreasing uncertainty as  $N$  increases.

**Generative process.** We fix the feature dimension  $p = 5$ . For each task  $t$ , we generate a sparse regression coefficient vector  $\beta_t \in \mathbb{R}^p$  with sparsity level  $k_t$ , where

$$\|\beta_t\|_0 = k_t, \quad k_t \in \mathcal{K} := \{5, 10, 15, \dots, 100\}.$$

The support set  $S_t \subset \{1, \dots, p\}$  with  $|S_t| = k_t$  is sampled uniformly at random. Conditional on  $S_t$ , the nonzero coefficients are drawn independently as  $(\beta_t)_j \sim \mathcal{N}(0, 3)$ ,  $j \in S_t$ , with  $(\beta_t)_j = 0$  for  $j \notin S_t$ . Conditioned on  $\beta_t$ , we generate a task-specific support set  $\mathcal{D}_t = \{(x_{t,n}, y_{t,n})\}_{n=1}^{N_t}$ , where covariates are sampled as  $x_{t,n} \sim \mathcal{N}(0, I_p)$  and responses follow the linear model

$$y_{t,n} = x_{t,n}^\top \beta_t + \varepsilon_{t,n}, \quad \varepsilon_{t,n} \sim \mathcal{N}(0, 1).$$

The number of observations per task is drawn uniformly as

$$N_t \sim \text{Discrete - Uniform}\{400, 401, \dots, 500\}.$$

**Model.** For each task  $t$ , we treat  $\mathcal{D}_t$  as an unordered set of tokens  $z_{t,n} = [x_{t,n}; y_{t,n}] \in \mathbb{R}^{p+1}$ . Tokens are embedded into  $\mathbb{R}^{d_{\text{model}}}$  and processed by an  $L$ -layer Transformer encoder ‘without positional encodings’, ensuring permutation equivariance across samples. A mean pooling operator produces a permutation-invariant task representation  $r_t$ , which is decoded by two heads: a magnitude head  $\hat{\beta}_{\text{mag},t} \in \mathbb{R}^p$  and a sparsity gate  $\hat{p}_t \in (0, 1)^p$ . The final coefficient estimate is

$$\hat{\beta}_t = \hat{\beta}_{\text{mag},t} \odot \hat{p}_t.$$

**Training objective.** Given a batch of  $M$  tasks, we minimize prediction error using soft gating:

$$\mathcal{L} = \frac{1}{M} \sum_{t=1}^M \left( \frac{1}{N_t} \sum_{n=1}^{N_t} (y_{t,n} - x_{t,n}^\top \hat{\beta}_t)^2 \right).$$

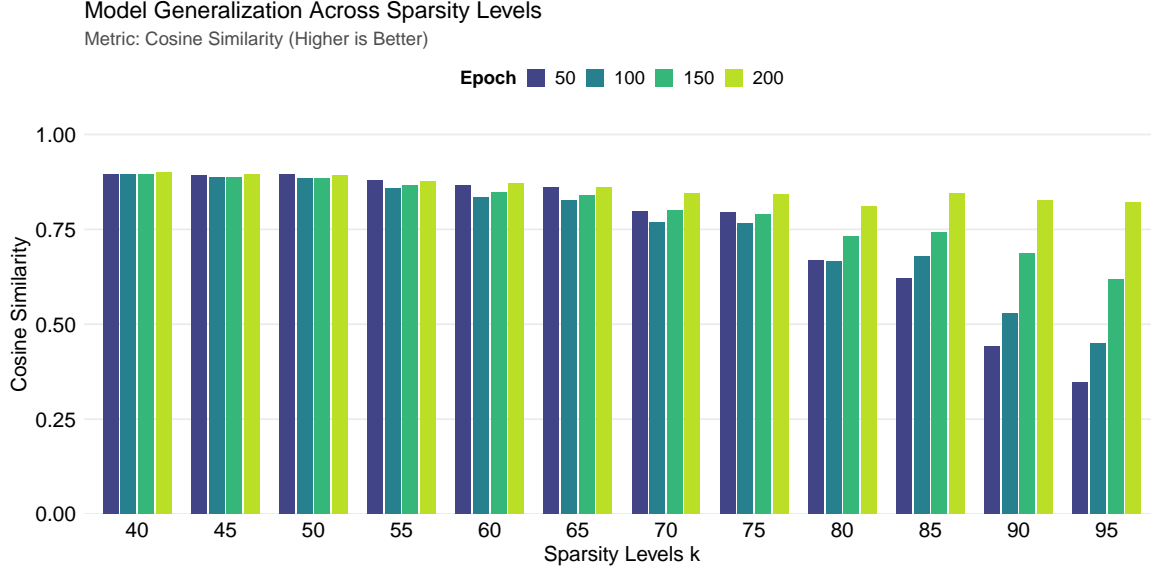


Figure 3: Cosine similarity between estimated and true regression coefficients across different sparsity levels. Here,  $k$  denotes the sparsity percentage, i.e.,  $k\%$  of the coefficients in the ground-truth parameter vector are zero. Bar clusters correspond to the performance evaluated at training epochs 50, 100, 150, and 200.

**Training meta-dataset construction.** We generate a fixed meta-dataset of  $T = 6000$  tasks spanning a grid of sparsity levels. Let

$$\mathcal{K} = \{5, 10, 15, \dots, 100\}$$

denote the set of sparsity levels. For each  $k \in \mathcal{K}$ , we generate 300 independent tasks, yielding  $T = 20 \times 300 = 6000$  tasks in total. Each task  $t$  is assigned a sparsity level  $k_t \in \mathcal{K}$  and is generated according to the sparse linear model described above.

**Per-task sampling.** For a task with sparsity level  $k_t$ , we sample a support set  $S_t \subset \{1, \dots, p\}$  with  $|S_t| = k_t$  uniformly at random, draw nonzero coefficients  $(\beta_t)_j \sim \mathcal{N}(0, 1)$  for  $j \in S_t$  (and  $(\beta_t)_j = 0$  otherwise), and then generate a support set  $\mathcal{D}_t = \{(x_{t,n}, y_{t,n})\}_{n=1}^{N_t}$ . The number of observations per task is drawn uniformly as  $N_t \sim \text{Discrete - Uniform}\{400, 401, \dots, 500\}$ , with covariates sampled as  $x_{t,n} \stackrel{\text{IID}}{\sim} \mathcal{N}(0, I_p)$  and responses generated as

$$y_{t,n} = x_{t,n}^\top \beta_t + \varepsilon_{t,n}, \quad \varepsilon_{t,n} \sim \mathcal{N}(0, 1).$$

**Train–test split.** After generating the full collection of  $T = 6000$  tasks, we randomly shuffle task indices and split tasks into  $T_{\text{train}} = 5400$  training tasks and  $T_{\text{test}} = 600$  held-out test tasks. All models are trained only on the training tasks; evaluation is performed on the held-out tasks.

**Performance.** Figure 3 reports across-epoch performance of the sparse recovery architecture under varying sparsity levels. We measure cosine similarity between the predicted

coefficient vector  $\hat{\beta}$  and the ground-truth  $\beta$ , where the sparsity parameter  $k$  denotes the percentage of zero coefficients in  $\beta$ . For moderate sparsity levels (e.g.,  $k \leq 60\%$ ), the model achieves high cosine similarity ( $> 0.85$ ) even at early training stages, indicating accurate recovery of the dominant signal components. As sparsity increases (larger  $k$ ), the recovery task becomes more challenging due to the reduced number of informative features. In these highly sparse regimes, performance at early epochs (e.g., epoch 50) is noticeably lower, reflecting difficulty in reliably identifying the small active support. However, continued training leads to consistent improvements across all sparsity levels. By epoch 200, the model attains high cosine similarity even when a large fraction of coefficients are zero, demonstrating that the sparsity gate progressively learns to isolate the relevant dimensions as optimization proceeds.

While cosine similarity captures point-estimation accuracy, it does not reflect the stability of the recovered coefficients across different realizations of the data. To assess the reliability of the estimator beyond point estimates, we analyze the empirical standard deviation of the predicted coefficients, denoted as  $\sigma(\hat{\beta})$ . Table 3 reports this quantity as a function of the support set size  $N$  across multiple sparsity percentages ( $k = 5, 20, 50, 80$ ). In low-sample regimes ( $N = 50$ ), uncertainty is elevated across all sparsity levels, particularly when sparsity is high, reflecting the difficulty of disentangling signal from noise with limited observations. As the number of observations increases, the standard deviation decreases monotonically for all sparsity levels. At  $N = 1000$ , uncertainty is uniformly low, indicating stable coefficient recovery even under extreme sparsity.

Table 3: Standard deviation of predicted regression coefficients  $\sigma(\hat{\beta})$  across varying support set sizes ( $N$ ) and sparsity percentages ( $k$ ). Here,  $k$  denotes the percentage of zero coefficients in the true parameter vector.

Support set size ( $N$ )	Sparsity percentage ( $k$ )			
	20	50	80	95
50	0.530	0.498	0.445	0.412
100	0.392	0.355	0.310	0.285
200	0.258	0.220	0.185	0.150
500	0.140	0.125	0.095	0.085
1000	0.062	0.055	0.048	0.042

#### 4.4 Topological Mismatch: Multimodal Posterior Inference

We next consider a setting in which the posterior distribution over task parameters exhibits a substantial topological mismatch relative to standard unimodal assumptions. In particular, we study amortized inference when the parameter distribution is highly multimodal and supported on a non-convex manifold. This experiment evaluates whether neural inference models can identify and represent disconnected posterior geometry using only observed input–output samples.

**Generative model.** Let  $\beta \in \mathbb{R}^2$  denote the task-specific regression parameter. We define a multimodal prior distribution consisting of  $K = 8$  Gaussian components arranged uniformly on a circle of radius  $R = 5.0$ :

$$p(\beta) = \frac{1}{K} \sum_{k=1}^K \mathcal{N}(\beta \mid \mu_k, \sigma^2 I_2), \quad \mu_k = R \begin{bmatrix} \cos\left(\frac{2\pi k}{K}\right) \\ \sin\left(\frac{2\pi k}{K}\right) \end{bmatrix}.$$

Conditioned on  $\beta$ , observations are generated according to the same linear model used throughout the paper

$$y_n = x_n^\top \beta + \varepsilon_n, \quad x_n \sim \mathcal{N}(0, I_2), \quad \varepsilon_n \sim \mathcal{N}(0, \sigma_\varepsilon^2),$$

yielding a task-specific dataset  $\mathcal{D} = \{(x_n, y_n)\}_{n=1}^N$ .

**Inference objective.** Given  $\mathcal{D}$ , the goal is to approximate the posterior distribution

$$p(\beta \mid \mathcal{D}),$$

which inherits the multimodal structure of the prior while being shaped by the likelihood induced by the observed  $(x, y)$  pairs. Notably, the inference model has access only to the observed samples and must identify the full posterior geometry without explicit knowledge of the prior components.

**Amortized conditional flow.** We employ a conditional normalizing flow trained via Conditional Flow Matching to learn a mapping from observed datasets to posterior distributions. The input dataset  $\mathcal{D}$  is first embedded into a fixed-dimensional context vector

$$\mathbf{r} = f_\psi(\mathcal{D}),$$

using a permutation-invariant encoder consistent with earlier experiments (Deep Sets). This representation summarizes the information contained in the observed  $(x, y)$  samples and conditions the inference model.

Let  $\beta_t \in \mathbb{R}^2$  denote the state of the flow at time  $t \in [0, 1]$ , initialized from a base distribution  $\beta_0 \sim \mathcal{N}(0, I_2)$ . The evolution of  $\beta_t$  is governed by a time-dependent velocity field

$$\frac{d\beta_t}{dt} = v_\phi(t, \beta_t, \mathbf{r}), \quad (9)$$

where  $v_\phi$  is a neural network parameterized by  $\phi$ . Integrating this ordinary differential equation yields

$$\beta_1 = \beta_0 + \int_0^1 v_\phi(t, \beta_t, \mathbf{r}) dt, \quad (10)$$

which represents a sample from the learned approximation to  $p(\beta \mid \mathcal{D})$ .

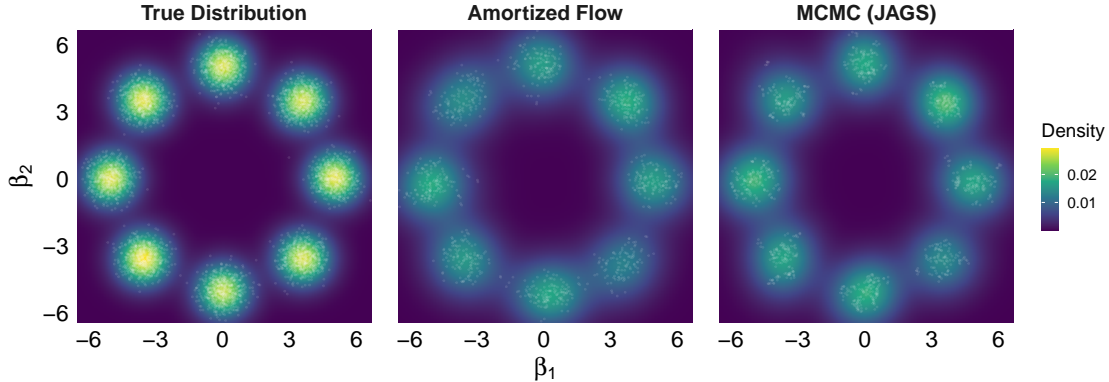


Figure 4: Posterior Sampling Benchmark: Visual comparison of the true multimodal distribution (Left), the Amortized Normalizing Flow approximation (Center), and the MCMC baseline (Right). The Amortized Flow successfully captures the complex multimodal geometry and separates the modes significantly faster than the baseline.

**Posterior geometry and transport dynamics.** Figure 4 compares samples from the true posterior distribution, the amortized flow approximation, and an MCMC baseline. The amortized model successfully allocates probability mass across all eight modes, demonstrating that it recovers the disconnected geometry of the posterior using only the observed  $(x, y)$  samples.

Figure 5 visualizes the transport induced by the learned vector field. Samples drawn from the isotropic Gaussian base distribution are smoothly transformed over time into the multimodal posterior structure, confirming that the model learns a continuous deformation that respects the topology of the target distribution.

**Computational efficiency.** In addition to capturing complex posterior geometry, the amortized flow provides substantial computational benefits. Posterior samples are generated in 0.82 seconds per task, compared to 2.76 seconds for the MCMC baseline, illustrating the advantage of amortized inference in repeated-task settings.

## 5 Discussion and Future Research

While our experiments confirm that neural networks possess a potent ability to learn hidden latent structures and approximate complex statistical functionals, this capability comes at a high cost. These architectures are inherently data-hungry, requiring vast quantities of synthetic samples to generalize effectively. Furthermore, while the neural estimators frequently achieved performance parity with classical frequentist methods, they lacked the ‘out-of-the-box’ reliability of standard algorithms. In many cases, achieving convergence required extensive hyperparameter fine-tuning, suggesting that while the theoretical capacity for inference exists, the practical implementation remains computationally demanding compared to analytical solutions.

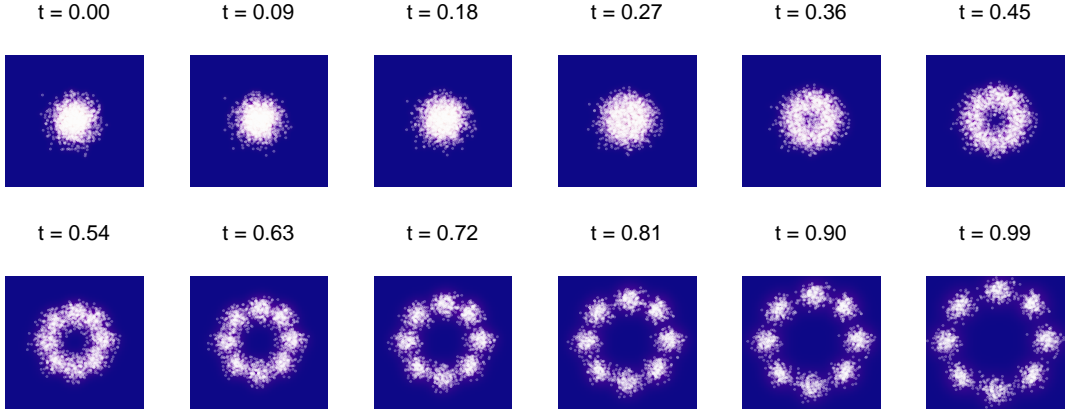


Figure 5: Visualization of the flow trajectory evolution. The horizontal panels illustrate the transformation of the initial particle distribution ( $\theta_0 \sim \mathcal{N}(0, I)$  at  $t = 0.00$ ) under the learned vector field over time. By  $t = 1.00$ , the particles have successfully converged to the target 8-mode posterior geometry.

The limitations of this approach were most evident in the sparse regression setting. Unlike unconstrained estimation, enforcing sparsity within a continuous optimization framework proved to be a delicate balancing act. The models were highly sensitive to the choice of loss function, often failing to converge to the true sparse support without meticulous calibration. This difficulty indicates that for tasks requiring strict structural constraints (such as variable selection), the standard gradient-descent paradigm requires further refinement to match the robustness of specialized algorithms like LASSO or SCAD.

Despite these hurdles, the amortized inference paradigm offers a compelling path forward, drawing parallels to the recent success of Large Language Models (LLMs). Just as LLMs leverage transfer learning to perform tasks they were not explicitly trained for, there is significant scope for developing ‘Large Statistical Models.’ A massive, pre-trained network exposed to a diverse universe of data-generating processes could potentially learn a universal representation of statistical inference. Such a model could be deployed for transfer learning on novel tasks, effectively amortizing the high initial training cost across thousands of distinct inference problems.

Finally, the deployment of these “black-box” estimators in scientific workflows calls for a much deeper understanding of their internal mechanisms. Future work should prioritize mechanistic interpretability, not only to explain how these networks produce parameter estimates, but also to understand how they generalize to out-of-sample prediction tasks. While amortization enables a single neural architecture to be deployed across a wide class of statistical problems, this convenience comes with a cost: the error behavior of the amortized procedure under different kinds of deployment shift remains largely uncharacterized. Studying such generalization error is fundamentally different from classical statistical risk analysis and needs new theoretical and empirical tools tailored to amortized inference.

## References

Raman Arora, Amitabh Basu, Poorya Mianjy, and Anirbit Mukherjee. Understanding deep neural networks with rectified linear units. In *International Conference on Learning Representations*, 2018. [5](#)

Andrew R Barron. Universal approximation bounds for superpositions of a sigmoidal function. *IEEE Transactions on Information theory*, 39(3):930–945, 1993. [5](#)

Leo Breiman. Statistical modeling: The two cultures. *Statistical Science*, 16(3):199–231, 2001. [2](#)

George Cybenko. Approximation by superpositions of a sigmoidal function. *Mathematics of Control, Signals and Systems*, 2(4):303–314, 1989. [5](#)

Alan E. Gelfand and Adrian F. M. Smith. Sampling-based approaches to calculating marginal densities. *Journal of the American Statistical Association*, 85(410):398–409, 1990. [2](#)

Samuel J Gershman and Noah D Goodman. Amortized inference in probabilistic reasoning. In *Proceedings of the 36th Annual Conference of the Cognitive Science Society*, 2014. [2](#)

David Greenberg, Marcel Nonnenmacher, and Jakob Macke. Automatic posterior transformation for likelihood-free inference. In *International Conference on Machine Learning*, pages 2404–2414. PMLR, 2019. [3](#)

Matthew Hoffman, Pavel Sountsov, Joshua V Dillon, Ian Langmore, Dustin Tran, and Srinivas Vasudevan. NeuTra-lizing Bad Geometry in Hamiltonian Monte Carlo Using Neural Transport. *arXiv preprint arXiv:1903.03704*, 2019. [3](#)

Kurt Hornik. Approximation capabilities of multilayer feedforward networks. *Neural Networks*, 4(2):251–257, 1991. [5](#)

Juho Lee, Yoonho Lee, Jungtaek Kim, Adam Kosiorek, Seungjin Choi, and Yee Whye Teh. Set transformer: A framework for attention-based permutation-invariant neural networks. In *International Conference on Machine Learning*, pages 3744–3753. PMLR, 2019. [3](#)

Yaron Lipman, Ricky TQ Chen, Heli Ben-Hamu, Maximilian Nickel, and Matt Le. Flow matching for generative modeling. In *International Conference on Learning Representations*, 2023. [3](#), [12](#)

Alexandra Sasha Luccioni, Sylvain Viguier, and Anne-Laure Ligozat. Estimating the Carbon Footprint of BLOOM, a 176B Parameter Language Model. *Journal of Machine Learning Research*, 24:1–15, 2023. [2](#)

Guido F Montufar, Razvan Pascanu, Kyunghyun Cho, and Yoshua Bengio. On the number of linear regions of deep neural networks. In *Advances in Neural Information Processing Systems*, volume 27, 2014. [5](#)

Elizbar A Nadaraya. On estimating regression. *Theory of Probability & Its Applications*, 9(1):141–142, 1964. [9](#)

Neel Nanda, Lawrence Chan, Tom Lieberum, Jess Smith, and Jacob Steinhardt. Progress measures for grokking via mechanistic interpretability. *arXiv preprint arXiv:2301.05217*, 2023. [7](#)

Radford M Neal. *Bayesian learning for neural networks*, volume 118. Springer Science & Business Media, 1996. [6](#)

George Papamakarios, Eric Nalisnick, Danilo Jimenez Rezende, Shakir Mohamed, and Balaji Lakshminarayanan. Normalizing flows for probabilistic modeling and inference. *Journal of Machine Learning Research*, 22(57):1–64, 2021. [3](#)

Alethea Power, Yuri Burda, Harri Edwards, Igor Babuschkin, and Vedant Misra. Grokking: Generalization beyond overfitting on small algorithmic datasets. *arXiv preprint arXiv:2201.02177*, 2022. [6](#)

Stefan T Radev, Marvin Schmitt, Valentin Pratz, Umberto Picchini, Ullrich Köthe, and Paul-Christian Bürkner. Neural methods for amortised parameter inference. *arXiv preprint arXiv:2404.12484*, 2024. [3](#)

Ali Rahimi and Benjamin Recht. Random features for large-scale kernel machines. In *Advances in neural information processing systems*, volume 20, 2007. [6](#)

Carl Edward Rasmussen and Christopher K I Williams. *Gaussian processes for machine learning*, volume 2. MIT press Cambridge, MA, 2006. [9](#)

Danilo Rezende and Shakir Mohamed. Variational inference with normalizing flows. In *International Conference on Machine Learning*, pages 1530–1538. PMLR, 2015. [3](#)

Jordan Richards, Matthew Sainsbury-Dale, Andrew Zammit-Mangion, and Raphaël Huser. Neural Bayes estimators for censored inference with peaks-over-threshold models. *Journal of Machine Learning Research*, 25(390):1–49, 2024. [3](#)

Håvard Rue, Sara Martino, and Nicolas Chopin. Approximate Bayesian inference for latent Gaussian models by using integrated nested Laplace approximations. *Journal of the Royal Statistical Society Series B: Statistical Methodology*, 71(2):319–392, 2009. [3](#)

Matthew Sainsbury-Dale, Andrew Zammit-Mangion, and Raphaël Huser. Likelihood-free parameter estimation with neural Bayes estimators. *The American Statistician*, 78(1):1–14, 2024. [2](#)

Matthew Sainsbury-Dale, Andrew Zammit-Mangion, Jordan Richards, and Raphaël Huser. Neural Bayes estimators for irregular spatial data using graph neural networks. *Journal of Computational and Graphical Statistics*, pages 1–16, 2025. [2](#)

Galit Shmueli. To explain or to predict? *Statistical Science*, 25(3):289–310, 2010. [2](#)

Ashish Vaswani, Noam Shazeer, Niki Parmar, Jakob Uszkoreit, Llion Jones, Aidan N Gomez, Łukasz Kaiser, and Illia Polosukhin. Attention is all you need. In *Advances in Neural Information Processing Systems*, volume 30, 2017. [8](#)

Edward Wagstaff, Fabian Fuchs, Martin Engelcke, Ingmar Posner, and Michael A Osborne. On the limitations of representing functions on sets. In *International Conference on Machine Learning*, pages 6487–6494. PMLR, 2019. [8](#)

Geoffrey S Watson. Smooth regression analysis. *Sankhyā: The Indian Journal of Statistics, Series A*, pages 359–372, 1964. [9](#)

Manzil Zaheer, Satwik Kottur, Siamak Ravanbakhsh, Barnabas Poczos, Russ R Salakhutdinov, and Alexander J Smola. Deep Sets. In *Advances in Neural Information Processing Systems*, volume 30, 2017. [3](#), [7](#)

Andrew Zammit-Mangion, Matthew Sainsbury-Dale, and Raphaël Huser. Neural methods for amortized inference. *Annual Review of Statistics and Its Application*, 12(1):311–335, 2025. [2](#)